Stable high-energy proton acceleration with water-leaf targets driven by intense laser pulses

L. R. He [1,*] M. Bachhammer [1,†] F. Balling [1] S. Biswas [1,2,3] L. Doyle [1] S. Gerlach [1] I. Hofrichter [1] M. Kharbedia [4] J. Liese [1] M. De Marco [5] T. Pohle [1] A. Praßelsperger [1] A.-K. Schmidt [1] F. Schweiger [1] M. F. Kling [1,2,3] S. Karsch [1,2] and J. Schreiber [1]

[1]*Ludwig–Maximilians–Universität München, Am Coulombwall 1, 85748 Garching, Germany*
[2]*Max-Planck-Institut für Quantenoptik, 85748 Garching, Germany*
[3]*SLAC National Accelerator Laboratory, Menlo Park, California 94025, USA*
[4]*Advanced Research Center for Nanolithography (ARCNL), Science Park 106, Amsterdam 1098 XG, Netherlands*
[5]*ELI ALPS, ELI-HU Non-Profit Ltd., Wolfgang Sandner utca 3, H-6728 Szeged, Hungary*

(Received 26 April 2024; revised 28 August 2024; accepted 25 April 2025; published 27 May 2025)

Laser plasma acceleration techniques hold promise for generating compact, high-flux relativistic proton bunches. However, the inherent instability of laser-plasma interactions and the requirement for reliable proton source stability often hinder their practical applications. In this paper, we explore the potential of a water-leaf target irradiated by 27 fs laser pulses with energies ranging from 1.1 to 9.9 J and peak intensities spanning from 10^{20} to 10^{21} W/cm^2. We finally conducted a series of 400 shots with a peak power of 300 TW, producing proton energies up to 30 MeV and peak flux beyond 10^9 protons MeV^{-1} msr^{-1}. These results demonstrate the possibility of long-term, stable, and efficient proton acceleration at high repetition rates, addressing a key challenge in laser-plasma acceleration.

DOI: 10.1103/PhysRevResearch.7.023190

I. INTRODUCTION

Advancements in laser technology over the past decades have ignited heightened interest in laser-driven ion acceleration as a compact and cost-effective complement to traditional radio-frequency (RF) accelerators. This type of particle acceleration broadens the application spectrum of conventional sources, unlocking possibilities in diverse fields such as science, technology, energy, and medicine [1–3]. Such applications can include neutron sources [4,5], material science [6–9], inertial fusion energy [10,11], and radiation biology [12–17].

In laser-driven ion acceleration, an intense laser pulse interacts with a target, rapidly ionizing its surface. Due to their much lighter mass, electrons are accelerated first within the laser field, gaining high kinetic energy. These energetic electrons move forward through the target and eventually escape into the vacuum from the rear surface. This displacement of electrons leaves behind positively charged ions, creating a strong electric field. This field can ionize surface contaminants on the rear side of the target and accelerate the resulting ions to high energies. This well-established mechanism is known as target normal sheath acceleration (TNSA) [18–20].

Although laser-accelerated ion beams typically exhibit a broad energy distribution, milestone experiments have demonstrated the capability of laser-driven ion acceleration to produce proton bunches with exceptional properties, including low emittance [21], small divergence of just a few degrees [22], monoenergetic energy spectra [23], and maximum energies of up to 150 MeV [24]. These attributes establish laser-driven ion acceleration as a significant tool for fundamental research and applications. However, while advances continue to push toward higher kinetic energies, the challenges of generating stable and efficient proton bunches and transitioning from singular proof-of-principle investigations to long-term, sustainable, repetitive operation remain a limitation for all applications of laser-driven ion acceleration.

Through the recent advancement in laser technology, laser pulses with peak power beyond 1 PW are accessible with repetition rates ∼1 Hz [25]. Online ion detectors are meanwhile available [26–29] and become integral parts in petawatt experiments [30–32]. A suitable high-repetition-rate target solution that is the source of ion bunches still represents a bottleneck. Different strategies have regained interest over the past years, for example, liquid crystals [33], prepositioned foils [34], tape drives [35,36], rotation solid targets [37], cryogenic jets [38,39], or near-critical gas target [40]. While these approaches have achieved notable success, the challenges of maintaining reliable and long-term operation (on the order of hours or more) for solid targets are particularly daunting, even at moderate repetition rates of ∼10 Hz.

Liquid jets [41] and particularly liquid-leaf targets have emerged as promising alternatives. These targets have been extensively tested and introduced into many systems [42–48], with scalability demonstrated to kilohertz repetition rates in

*Contact author: He.Lianren@physik.uni-muenchen.de
†Contact author: M.Bachhammer@physik.uni-muenchen.de

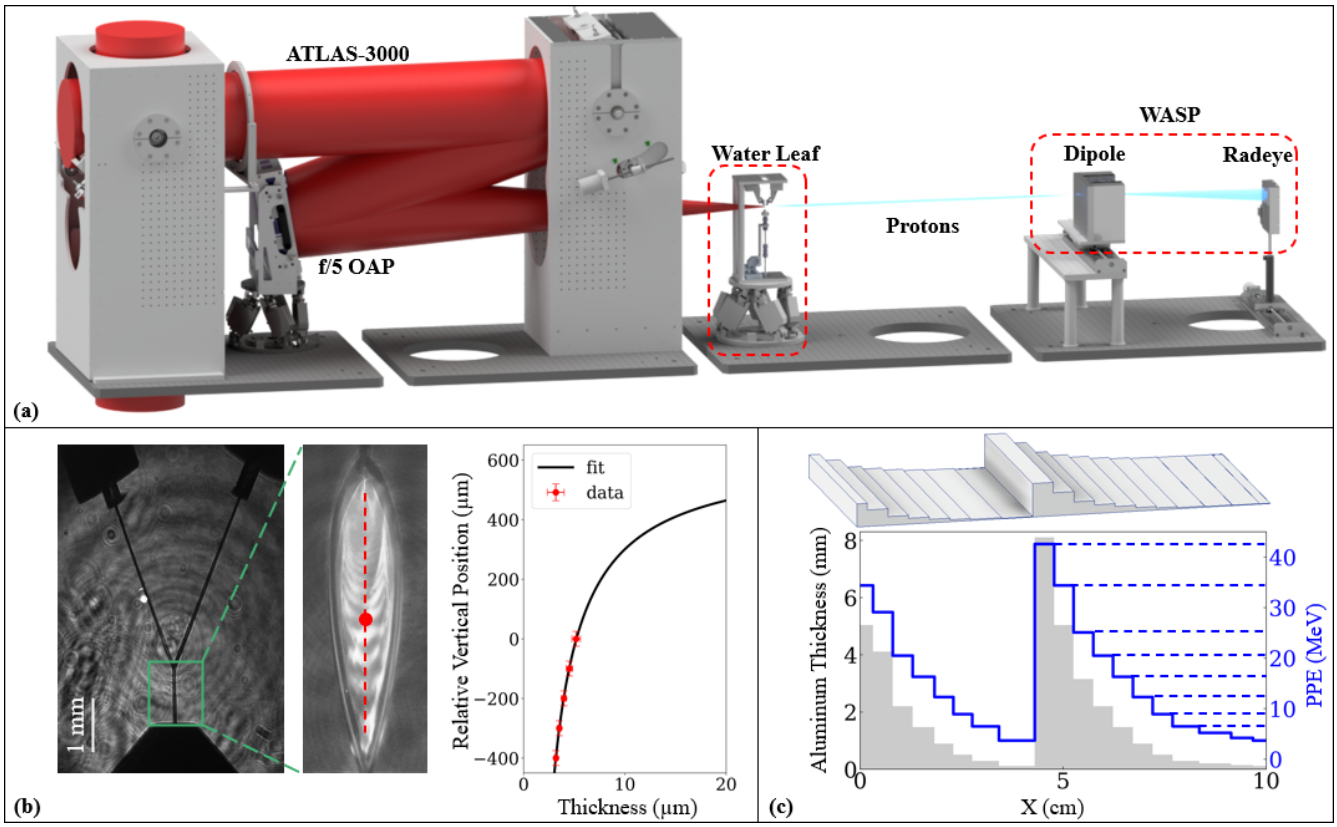

FIG. 1. (a) Schematic of the experimental setup. (b) Dimensions of the water-leaf target. A magnified false-color image highlights the target, with the laser-target interaction point indicated by a red dot at an approximate thickness of $5 \pm 0.4\,\mu$m. The thickness was measured at five positions along the vertical central axis (red dashed line) using white light spectral interference techniques [49,50]. Then the thickness profile was fitted according to the model by Taylor [51], where thickness is inversely proportional to the distance from the colliding point. Measurement errors of 5–8% are obscured by the data points, primarily due to the 25 μm spot size of the white light source on the water-leaf target. (c) Schematic of the aluminum phantom with varying strip thickness from 0.1 to 8.1 mm and corresponding proton penetration energy (PPE) from 3.7 to 42.6 MeV.

earlier studies [43], albeit at modest laser energies. Liquid-leaf targets offer several unique advantages, including cost efficiency, debris-free operation, a wide range of tunable thicknesses, near-solid density, and particularly the capacity for long-term continuous operation. These attributes make them highly attractive as a high-repetition-rate target solution for laser-driven ion acceleration. Despite their promise, recent experiments have achieved only modest results, with proton or deuteron bunch energies reaching just a few megaelectronvolts [44,45,52]. These limitations currently hinder their application in advanced technologies such as neutron production, material science, and radiation biology, where higher proton energies and fluxes are essential.

In this paper, we present experimental results on proton acceleration using a water-leaf target at the 300 TW level. Our analysis concentrates on the scaling of maximum proton energy on laser pulse energy, which we varied actively, as well as on the effects of repetition rate and different laser-target interaction positions on proton bunch stability. Most importantly, we demonstrate the feasibility of generating a 20 MeV (some shots up to 30 MeV), 0.1 Hz proton source using water-leaf targets. More than 400 shots were recorded, and shot-to-shot variations of the proton bunch parameters, specifically the maximum energy and particle flux, were analyzed statistically. By achieving long-term, stable, and efficient proton acceleration at high repetition rates, in this paper, we tackle one of the key challenges in the field of laser-plasma acceleration, advancing the development of reliable laser-driven ion sources for real-world applications.

II. EXPERIMENTAL SETUP

The experiments were conducted on the Advanced Titanium-sapphire LAser System (ATLAS-3000) at the Centre for Advanced Laser Applications (CALA), Garching, Germany. Figure 1(a) illustrates the schematic of the setup. In the experiments presented, the laser delivered energy of up to 16.5 J before compression, with a central wavelength of 800 nm (λ). With consideration of compression and transport losses, the measured laser transmission is 60%, resulting in 9.9 J of laser energy on target, with a pulse duration of 27 fs full width at half maximum (FWHM; τ). The *s*-polarized laser beam was then focused to a 5.3 μm FWHM diameter focal spot (d_{FWHM}) and directed onto the water leaf at an incident angle of 6.8° by an f/5 off-axis parabolic (OAP) mirror. The corresponding peak intensity is 1.1×10^{21} W/cm^2 ($a_0 \approx 18.6$) when assuming a Gaussian beam profile. It is noteworthy that this assessment tends to overestimate the peak

intensity of the actual laser beam profile by at least a factor of 1.5 [53], e.g., due to the detection limit inherent in the low-dynamic-range images of the attenuated focus profile. The repetition rate of laser was up to 1 Hz, and the measured laser contrast was 10^{10} up to 200 ps before the pulse peak, decreasing exponentially to 10^5 at 1 ps before the pulse peak.

The planar water-leaf target was precisely positioned in the attenuated laser focal spot using a microscope (not shown) and a six-axis hexapod. An automated online wide-angle spectrometer (WASP) [54], equipped with a calibrated large-area pixelated semiconductor detector (Radeye [27]), was positioned in the target normal downstream direction for the measurement of proton spectra. This diagnostic captures proton bunches through a slit, providing larger detection angles than traditional pinhole-based Thomson parabola spectrometer [55,56].

The planar water-leaf target was created by precisely colliding two 50-μm-diameter water jets at a full angle of 45°, each flowing at a rate of 1.5 mL/min, as illustrated in Fig. 1(b). Typically, multiple water-leaf targets are produced in a sequence resembling a chain. The initial water leaf is oriented perpendicular to the plane of the nozzles, with subsequent leaves maintaining orthogonal alignment to the preceding ones. This configuration continues until the water leaf disintegrates into droplets and spray. The first water leaf measured ∼1 mm in length and 0.3 mm in width, with thicknesses ranging from 3 to 20 μm depending on the vertical position, as depicted in Fig. 1(b). The target thickness ranged from 3 to 5 μm. The precise alignment between the nozzles was achieved using two motorized linear piezostages, maintaining a few millimeters distance between the nozzles and the water-leaf target. The target operated under background pressures ranging from 1.0×10^{-4} to 1.0×10^{-3} mbar. To prevent potential damage to sensitive beamline and laser optics from water vapor, an optical window constructed of TurboFilm (Baader Planetarium GmbH) with a thickness of 12 μm was inserted between the beamline and experiment chamber. Additionally, a compact heated catcher, inspired by the hotend design of three-dimensional (3D) printers and maintained at a temperature between 100 and 120 °C, was consistently positioned at the end of the first water leaf to facilitate the removal of water from the chamber and prevent freezing of the water-leaf target.

The target system operated robustly in a vacuum for >10 h. The integration of the hexapod and linear stages provided a high degree of freedom to control the position of the target prior to the next shot. This adaptability also allowed for comprehensive scans of the target position, including movements along the laser axis, vertical adjustments (varying target thickness), and correcting for rotational variations between shots. Such flexibility played a crucial role in identifying the optimal interaction position that resulted in large proton energy, particle yield, and stable operation.

The WASP allowed online detection of the energy spectra and angular distribution of laser-accelerated ions. For on-shot energy calibration, an aluminum mask consisting of stripes with varying material thickness was placed in front of the Radeye detector. The schematic of the aluminum phantom with varying strip thickness from 0.1 to 8.1 mm and

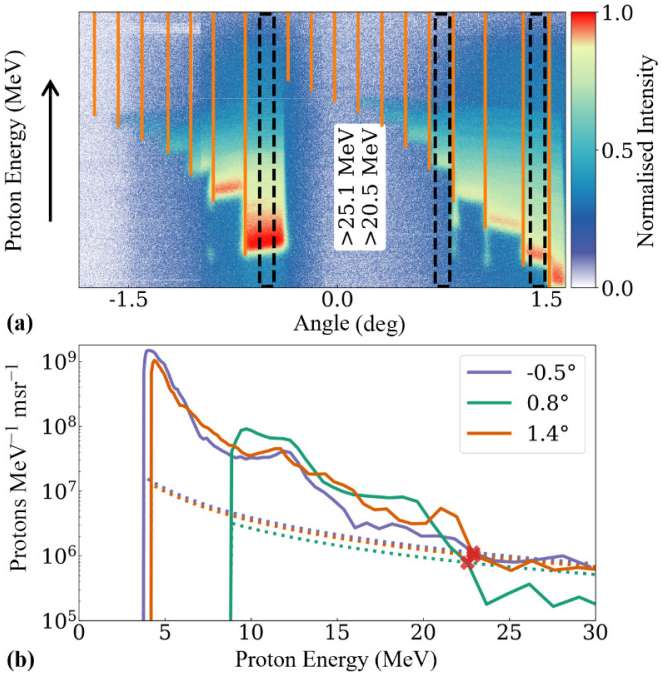

FIG. 2. (a) Typical stairlike proton spectra obtained from the Radeye detector for 8.4 J laser energy. The columns between orange lines represent the position of an aluminum phantom with varying thicknesses, where uplifted signal onset indicates thicker aluminum, correlating with higher penetrating energy. Black dashed rectangles correspond to different angular positions, specifically −0.5°, 0.8°, and 1.4°, with the normal direction of the target at 0°. (b) Reconstructed spectra for different angular positions (see the figure legend); solid and dotted lines represent spectra and noise levels, respectively.

corresponding proton penetration energy (PPE) from 3.7 to 42.6 MeV is shown in Fig. 1(c).

Figure 2(a) displays a typical recorded image for 8.4 J laser energy where the magnetic field causes protons to deflect downwards. The orange lines indicate the positions of the aluminum stripes. Uplifted signal onset indicates thicker aluminum, implying higher penetration energy. The resulting image illustrates the typical staircase structure of the proton spectrum due to the presence of the phantom which modulates the broad energy distribution [54]. The incorporation of the phantom provided immediate insights into ion performance, particularly concerning the maximum proton energy. For example, in Fig. 2(a), a swift determination of the maximum proton energy >20.5 MeV but remaining <25.1 MeV was evident. The full angular resolution was impeded by the phantom. Proton spectrum could be reconstructed at different angular positions, such as −0.5°, 0.8°, and 1.4°, with the normal direction of the target at 0°, represented by the three black rectangles in Fig. 2(a). The solid lines in Fig. 2(b) illustrate the reconstructed spectrum with particle yields reaching up to 1.0×10^9 protons MeV^{-1} msr^{-1}. The intersection of the spectrum with the noise level (dotted lines) signifies the maximum proton energy being ∼23 MeV, in good agreement with the swift determination via the phantom. The thickness of the phantom was insufficient to fully exclude signals from oxygen ions, particularly for the thinnest strip with a 0.1 mm thickness, which corresponds to a penetrating energy of

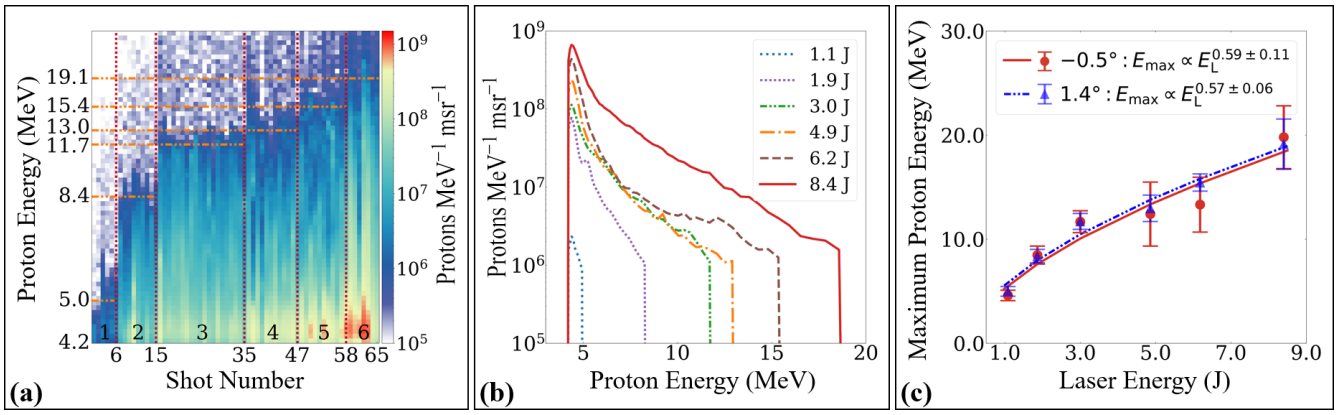

FIG. 3. (a) Proton spectra of 65 shots at 1.4° with a detectable minimum proton energy of 4.2 MeV. The spectra are sorted into six groups labeled from 1 to 6 (separated by red dotted lines) representing different laser energy settings: 1.1, 1.9, 3.0, 4.9, 6.2, and 8.4 J, respectively. The orange dash dotted lines correspond to the average maximum proton energy for each laser energy setting. Note that the *y* axis is nonlinear. (b) Average proton spectra for each laser energy (indicated as color code). (c) Maximum proton energy as a function of the laser energy. The average data points with standard deviation are displayed in blue and purple for −0.5° and 1.4°, accompanied by power-law fits at each laser energy.

122 MeV for O^{+8} ions. However, due to the effect of the magnetic field on particle deflection, which is inversely proportional to the Larmor radius ($y_d \propto Bq/mv$), signals from oxygen ions and protons are detected at distinct vertical positions on the detector [54]. Calculations, considering a maximum proton energy of 30 MeV and a minimum detectable energy of 122 MeV for O^{+8} ions, show no overlap between these signals.

III. RESULTS

The maximum proton energy (E_{max}) was measured as a function of laser energy, ranging from 1.1 to 8.4 J on target by sequentially turning on amplifiers. This corresponded to an intensity (I_0) ranging from 1.2×10^{20} to 9.2×10^{20} W/cm^2, for the same nominal laser-target interaction position and laser pulse duration. A total of 65 shots were executed in shot-on-demand mode, systematically organized into six groups according to the laser energy, as depicted in Fig. 3(a). An evident increase in the average maximum proton energy, ascending from 5.0 to 19.1 MeV, was observed in response to the incremental adjustments in laser energy. The average energy spectra in Fig. 3(b) underline this trend. Additionally, the particle yield exhibits a significant increase with the rise in laser energy. Figure 3(c) presents the maximum proton energies of all 65 shots as a function of laser energy. Two power-law fits are displayed for −0.5° and 1.4°, yielding the scaling relation $E_{max} \propto E_L^{0.59\pm0.11}$ and $E_{max} \propto E_L^{0.57\pm0.06}$, respectively.

A second experimental campaign was conducted to investigate the effect of repetition rate on ion acceleration stability. In this campaign, 26 additional shots were recorded at a constant laser energy of 5.1 J, operating in burst mode. The shots were categorized by repetition rates as follows: shots 1–9 were conducted at 0.1 Hz, shots 10–18 at 0.2 Hz, and shots 19–26 at 0.3 Hz (limited by the readout speed of the Radeye).

Figure 4(a) shows proton spectra extracted at three distinct angular positions (−0.5°, 0.8°, and 1.4°). Given the critical role of energy and flux stability in assessing acceleration performance, our investigation focused on proton energy and proton flux as the primary output parameters. The data points in Fig. 4(b) represent the maximum proton energy for each shot, while Fig. 4(c) illustrates the proton flux at 10 MeV. The shaded areas indicate the standard deviations ($\pm\sigma$) around the mean (μ), represented by the dotted line.

The average maximum proton energy and standard deviation of three distinct angular positions is 15.7 ± 1.1 MeV at 0.1 Hz, 14.9 ± 0.6 MeV at 0.2 Hz, and 15.4 ± 0.4 MeV at 0.3 Hz. A similar trend is observed for proton flux at 10 MeV. The average proton flux at 10 MeV remains stable for repetition rates from 0.1 to 0.3 Hz, $\sim(1.0 \pm 0.2) \times 10^7$ protons MeV^{-1} msr^{-1}. These results, depicted in Fig. 4, suggest that the repetition rate is not a limiting factor for stable proton performance.

Based on these observations, we conducted over 400 shots at a repetition rate of 0.1 Hz. For this experimental campaign, the flow rate was increased to 3.2 mL/min, resulting in a longer target with a thickness of $\sim 3 \pm 0.2$ μm in this central region. Proton bunches were continuously generated with laser energy between 9.8 and 10.1 J, with an average of 9.9 J. The angle of −0.5°, close to the target normal direction, was analyzed for the shot-to-shot variation studies, as it provides the broadest detectable range of proton energies. Statistical analyses were conducted on the entire dataset, and the results are presented in Fig. 5. This setup achieved a maximum proton energy of up to 30 MeV and a peak flux of $\sim 10^9$ protons MeV^{-1} msr^{-1}, as depicted in Fig. 5(a). The gaps in the spectral data correspond to manual pauses in laser shooting due to the temporary nonoperational state of the camera used for monitoring target alignment. These interruptions did not affect the consistency of the experimental setup or the subsequent data collection.

Figure 5(b) shows the maximum proton energy which averages to 22.0 ± 3.1 MeV considering all shots. The proton flux is evaluated at 17 MeV because all shots delivered energies beyond that value and is $(3.5 \pm 1.6) \times 10^6$ protons MeV^{-1} msr^{-1}. A Pearson correlation analysis was performed to examine the potential relationship between maximum proton energy and the corresponding particle yield at

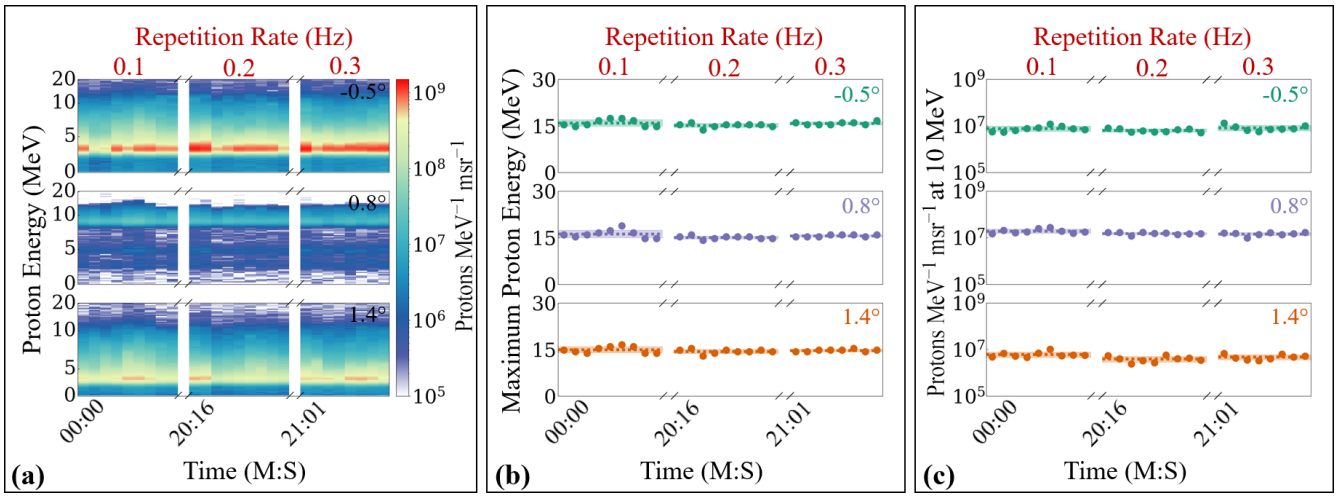

FIG. 4. The effect of repetition rate on ion acceleration stability. (a) Proton spectra evaluated at three different angular positions, all conducted at a laser energy of 5.1 J. (b) and (c) depict the maximum proton energy and particle yield at 10 MeV, respectively. The shaded regions represent the standard deviation ($\pm\sigma$) around the mean (dotted lines).

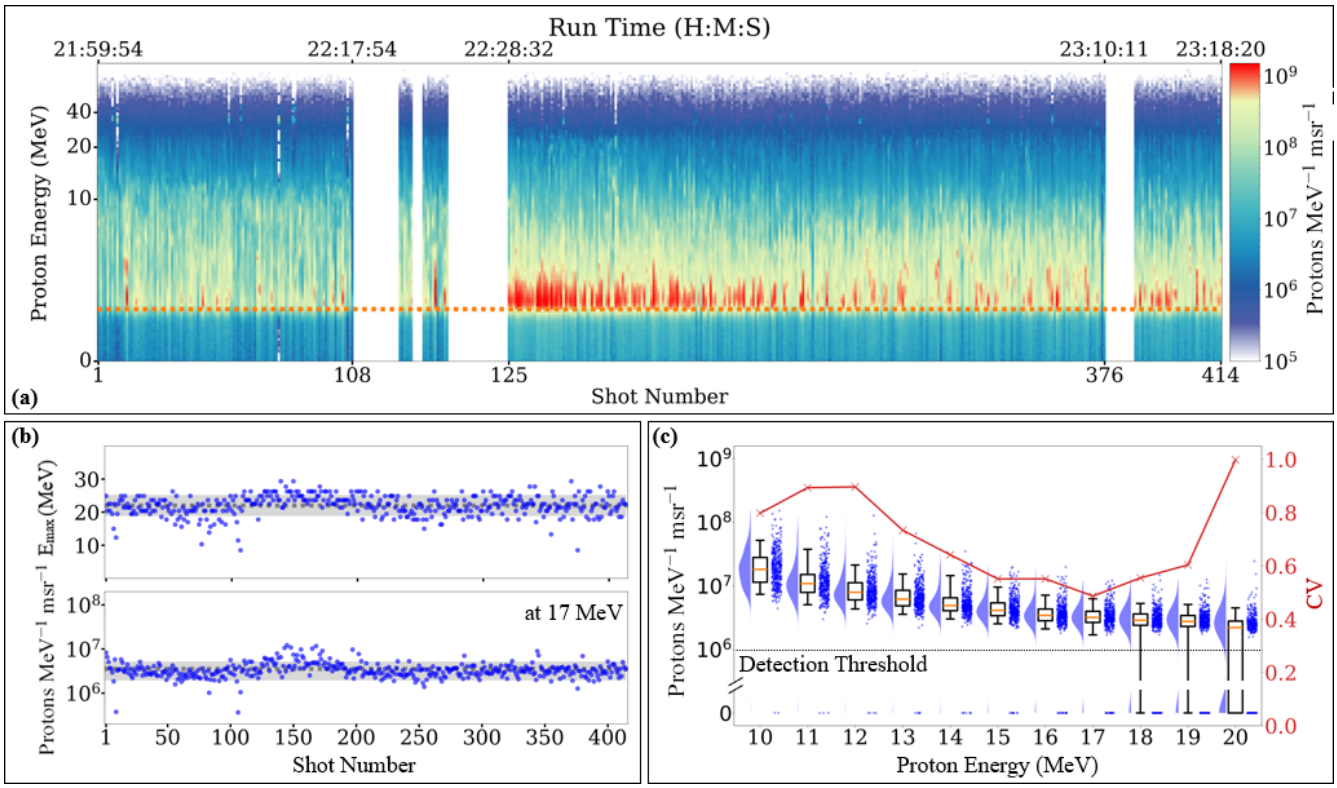

FIG. 5. Shot-to-shot variation study near the target normal direction (at $-0.5°$). (a) Proton spectra obtained from >400 shots at 0.1 Hz with an average laser energy of 9.9 J. All data were collected over a duration of 1 h, 18 min, and 26 s, with a total of 9 min and 26 s of recorded gaps. The gaps in the spectral data correspond to manual pauses in laser shooting due to a temporary nonoperational state of the camera used for monitoring target alignment. The orange solid lines indicate the minimum detectable proton energy of 3.7 MeV, constrained by the presence of a phantom positioned in front of the detector. The maximum proton energy achieved is up to 30 MeV, with a peak flux beyond 10^9 protons $\mathrm{MeV}^{-1}\,\mathrm{msr}^{-1}$. (b) Statistical analysis of the maximum proton energy and proton flux at 17 MeV (averaged to $0.8E_{\mathrm{max}}$) for all shots. (c) Probability density and discrete distribution of proton counts at specific energies across all shots. Rain plots are employed to reduce overlap and enhance the clarity of experimental data visualization. Each set of rain-cloud plots corresponds to the same energy level. The dataset is also represented using half-violin (cloud) and box plots for statistical evaluation, with the whiskers of the box plots extending to [5%, 95%] of the data range. The red solid lines depict the coefficient of variation (CV) of the particle yield at specific energies, aligned with the right y axis. The dotted line marks the detection threshold of the WASP.

17 MeV across all 400 shots. The Pearson correlation coefficient was 0.6, indicating that the variations in maximum proton energy exhibit a modest correlation with the particle flux at 17 MeV.

In Fig. 5(b), we only illustrate the particle flux at 17 MeV. Further investigation, particularly at other selected energies in 1 MeV steps across the broad spectrum, is warranted. Figure 5(c) facilitates this analysis by employing a rain-cloud plot, which provides an overview of the proton spectra variations across >400 shots at 9.9 J. In this plot, the proton flux at a given energy, such as 10 MeV, is determined for each shot, resulting in data points (rain). The vertical filled curve (cloud) represents the histogram of these data points. Additionally, the data are presented as a box plot, where the interquartile range (IQR) contains 50% of the data points, serving as a visual indicator of variations in the data distribution. The orange lines within the IQR denote the median, offering insight into the central tendency of the dataset. The medians of the box plots reveal typical exponential energy spectra. Specifically, from 20 to 10 MeV, the particle yield increases from 10^6 to 10^8 protons MeV^{-1} msr^{-1}.

An increasing trend in the number of shots falling below the detection threshold for higher proton energies is observed. Additionally, the coefficient of variation ($\mathrm{CV} = \sigma/\mu$) is calculated for each energy and represented by the red solid curve. It ranges from 50% to 100%, with an average of 70%, and is minimal at ∼17 MeV, corresponding to 77% of the average $E_{\max}$.

IV. DISCUSSION

In this paper, we provide a more comprehensive understanding of the scaling relationship between maximum proton energy and laser energy at two different angles, where the thinnest strips stood, offering detectable proton energies as low as 3.7 and 4.2 MeV. In contrast, thicker aluminum strips positioned in front of the detector at other angles increase the detectable proton energy threshold, filtering out lower-energy protons, particularly at lower laser energies, and leading to systematic errors. The scaling relationship at -0.5° $E_{\max} \propto E_L^{0.59\pm0.11}$ aligns well with the scaling at 1.4° $E_{\max} \propto E_L^{0.57\pm0.06}$, indicating a much larger overall divergence of the protons. This result closely matches the empirical scaling law proposed by Zimmer *et al.* [57], $E_L^{0.59}$. We observed larger fluctuations in maximum proton energy and flux for laser energies >3 J, despite conducting the experiment in shot-on-demand mode with consistent target conditions and maintaining laser energy stability ∼1%. These fluctuations were primarily attributed to the shot-to-shot stochastic behavior of the laser system, influenced by unknown parameters such as contrast, focus pointing, and wavefront.

During the second experimental campaign, proton bunch performance remained stable when targeting the middle segment of the water leaf with variations in repetition rate having no significant impact on the proton bunches. This stability is likely due to the 0.3 Hz operation rate being well below the resonance frequency of the water leaf [48], insufficient to induce substantial fluctuations in the position of the water leaf.

To this end, a series of 400 shots were recorded at 0.1 Hz with an average laser energy of 9.9 J incident onto the middle of the water-leaf target, achieving higher proton maximum energy, enhanced particle flux, and improved shot-to-shot stability. The experiment was limited to >400 shots solely due to time constraints, as the campaign extended late into the evening. Remarkably, our results represent a state-of-the-art advancement, achieving a fivefold increase in maximum proton energy (from 6 to 30 MeV, corresponding to an increase in penetration depth in water from 0.5 to 8.8 mm) and a more than three-orders-of-magnitude improvement in particle flux compared with previous achievements with similar targets [43–45,52].

Table I highlights a comparison of key quantities of laser-proton acceleration using similar water-leaf targets. For example, Puyuelo-Valdes *et al.* [44] demonstrated 3.5 MeV protons with a laser pulse energy of 4 J, duration of 30 fs, and a focal spot size of 20 μm. Treffert *et al.* [45] reported 4.4 MeV deuterons with a laser pulse energy of 5.5 J, duration of 45 fs, and a tight focus of 1.8 μm, i.e., an intensity exceeding 10^{21} $\mathrm{W/cm}^2$. Recently, Streeter *et al.* [52] generated 6 MeV proton beams with a laser pulse energy of only 190 mJ, duration of 57 fs, and a focus of 1.2 μm. This suggests a complicated dependency, where the smallest focal spot and highest intensity may not necessarily yield the maximum ion energies. The laser pulse energy appears to play the more important role [58]. The realization of these advancements is not only a matter of increasing the laser energy but also of facing the technical challenges that come with it. These challenges include mitigating the interference from stronger electromagnetic pulses during laser-plasma interactions [59] and managing the increased sonic pressure that impacts target stability [60]. Despite these hurdles, the reproducibility and reliability of a proton source capable of long-term operation are demonstrated.

Although Dover *et al.* [36] reported similar results to this paper using solid targets, reliably shooting targets thinner than 5 μm with a tape system seems difficult. In contrast, the thickness of water-leaf targets can be reduced to 200 nm [48], presenting substantial advantages for more efficient ion acceleration mechanisms such as radiation pressure acceleration (RPA) [61–63].

Another question arises though regarding shot-to-shot variations in proton energy. If the variation of maximum energy $dE_{\max}$ was solely due to fluctuations of laser energy dE_L according to the scaling, we would expect that $dE_{\max}/E_{\max} = 0.57 dE_L/E_L$. However, the relative variation of maximum proton energy in this paper is up to 14% in Fig. 5(b), while the laser energy varies only by 0.5%, hinting at the influence of other, as yet unknown, factors that warrant further investigation. Despite these variations, the maximum proton energy remained consistent throughout the experiment, underscoring the robustness and reproducibility of proton bunch generation, even under fluctuating laser system conditions and other so far uncontrollable parameters that typically degrade performance. However, the particle flux, particularly near the maximum proton energy, proved more sensitive to these degradations. This sensitivity often led to an increasing number of shots falling below the detection threshold for higher proton energies, causing the trend toward greater variation at higher proton energies as reflected by the CV value in Fig. 5(c). Therefore, the reliability in applications likely benefits from

TABLE I. Comparison of experimental parameters and results with previous studies using water-leaf targets.

Reference	Puyuelo-Valdes *et al.* [44]	Treffert *et al.* [45]	Streeter *et al.* [52]	This paper
Ions	Protons	Deuterons	Protons	Protons
E_L (J)	4.0	5.5	0.19	9.9
d_{fwhm} (μm)	19.5	1.8	1.2	5.3
τ_{fwhm} (fs)	30	45	57	27
I_{peak}	4.0×10^{19}	1.2×10^{21}	3.5×10^{19}	1.1×10^{21}
l (μm)	5 ± 1 & 1 ± 0.5	5 ± 1	0.6 ± 0.1	3 ± 0.2
E_{max} [Avg. E_{max}] (MeV)	4.0 [3.5]	4.4 [N/A]	6 [N/A]	30 [22]
Flux at 4 MeV (N MeV^{-1} msr^{-1})	$\sim 10^6$	$\sim 10^6$	$\sim 10^8$	$\sim 10^9$
Flux at 17 MeV (N MeV^{-1} msr^{-1})	N/A	N/A	N/A	5×10^6
No. consecutive shots	60	60	300	252

conservative energy selection around minimal CV; in our case, this is at 70–80% of average E_{max}.

V. CONCLUSION AND OUTLOOK

In conclusion, in this paper, we present an exploration of operating a water-leaf target system and basic online diagnostics for proton bunches, demonstrating its feasibility at a repetition rate of 0.1 Hz for >400 shots at a peak power level of 300 TW. The demonstrated stability and performance of proton bunches represent a crucial step toward practical laser-driven ion sources, opening possibilities for applications requiring reliable high-energy proton bunches. Additionally, with the development of state-of-the-art (high-energy and high-repetition-rate) laser systems, the potential for water-leaf targets to scale to kilohertz operation is extremely exciting.

As a conservative estimate, our scaling implies the potential to generate >60 MeV protons with the full ATLAS-3000 energy of 60 J on target, assuming identical target thickness and focal spot size. Given recent developments with plastic targets, significant improvements through optimization of target thickness and stronger scaling are likely [24].

An important direction for future research in proton bunch stabilization is the development of auto-optimized laser systems and target systems. This capability would allow exploiting the full 1 Hz repetition rate of our laser system and can pave the way for the future integration of feedback loops and fine-tuning of the laser and target system, aiming at meeting the stringent requirements of proton bunch performance for applications. To realize such stable proton bunches, it will be crucial to establish the underlying correlations by incorporating real-time diagnostics for both target parameters and laser at full power. Additionally, stabilization could be enhanced through the application of machine-learning techniques [64] and optimization methodologies such as Bayesian approaches [65].

ACKNOWLEDGMENTS

We thank T. Rösch, J. Hartmann, E. Chowdhury, P. Puyuelo-Valdes, G. Gatti, G. Schaumann, Z. X. Cao, Z. Y. Peng, Y. Gao, W. J. Ma, X. Chen, J. H. Bin, and Z. J. Sui for fruitful discussions. We appreciate the support from the workshops, technical, IT, and engineering (design) groups of Ludwig-Maximilians-Universität München (LMU) and CALA. L.R.H. is supported by the China Scholarship Council within the joint LMU-CSC program. L.D. acknowledges the support of the German Research Foundation (DFG) within Project No. FOR 2783. J.L. acknowledges the support of the DFG within Project No. 491853809. A.P. acknowledges the support of the Konrad-Adenauer-Stiftung and the BMBF within Project No. 05P21WMFA1. A.K.S. is supported by GSI within the R&D project GSI-LMSCH2025 with the LMU. M.B. and F.S. acknowledge the support of the BMBF within Project No. 01IS17048.

[1] H. Daido, M. Nishiuchi, and A. S. Pirozhkov, Review of laser-driven ion sources and their applications, Rep. Prog. Phys. **75**, 056401 (2012).

[2] A. Macchi, M. Borghesi, and M. Passoni, Ion acceleration by superintense laser-plasma interaction, Rev. Mod. Phys. **85**, 751 (2013).

[3] J. Schreiber, P. Bolton, and K. Parodi, Invited review article:"hands-on" laser-driven ion acceleration: A primer for laser-driven source development and potential applications, Rev. Sci. Instrum. **87**, 071101 (2016).

[4] M. Roth, D. Jung, K. Falk, N. Guler, O. Deppert, M. Devlin, A. Favalli, J. Fernandez, D. Gautier, M. Geissel *et al.*, Bright laser-driven neutron source based on the relativistic transparency of solids, Phys. Rev. Lett. **110**, 044802 (2013).

[5] Y. L. Yao, S. K. He, Z. Lei, T. Ye, Y. Xie, Z. G. Deng, B. Cui, W. Qi, L. Yang, S. P. Zhu *et al.*, High-flux neutron generator based on laser-driven collisionless shock acceleration, Phys. Rev. Lett. **131**, 025101 (2023).

[6] P. K. Chu, J. Chen, L. Wang, and N. Huang, Plasma-surface modification of biomaterials, Mater. Sci. Eng. R Rep. **36**, 143 (2002).

[7] B. Dromey, M. Coughlan, L. Senje, M. Taylor, S. Kuschel, B. Villagomez-Bernabe, R. Stefanuik, G. Nersisyan, L. Stella, J. Kohanoff *et al.*, Picosecond metrology of laser-driven proton bursts, Nat. Commun. **7**, 10642 (2016).

[8] M. Barberio, M. Scisciò, S. Vallières, F. Cardelli, S. Chen, G. Famulari, T. Gangolf, G. Revet, A. Schiavi, M. Senzacqua *et al.*, Laser-accelerated particle beams for stress testing of materials, Nat. Commun. **9**, 372 (2018).

[9] W. Redjem, A. J. Amsellem, F. I. Allen, G. Benndorf, J. Bin, S. Bulanov, E. Esarey, L. C. Feldman, J. Ferrer Fernandez, J. Garcia Lopez *et al.*, Defect engineering of silicon with ion pulses from laser acceleration, Commun. Mater. **4**, 22 (2023).

[10] M. Roth, T. E. Cowan, M. H. Key, S. P. Hatchett, C. Brown, W. Fountain, J. Johnson, D. M. Pennington, R. A. Snavely, S. C. Wilks *et al.*, Fast ignition by intense laser-accelerated proton beams, Phys. Rev. Lett. **86**, 436 (2001).

[11] O. A. Hurricane, P. K. Patel, R. Betti, D. H. Froula, S. P. Regan, S. A. Slutz, M. R. Gomez, and M. A. Sweeney, Physics principles of inertial confinement fusion and us program overview, Rev. Mod. Phys. **95**, 025005 (2023).

[12] T. Ostermayr, C. Kreuzer, F. Englbrecht, J. Gebhard, J. Hartmann, A. Huebl, D. Haffa, P. Hilz, K. Parodi, J. Wenz *et al.*, Laser-driven x-ray and proton micro-source and application to simultaneous single-shot bi-modal radiographic imaging, Nat. Commun. **11**, 6174 (2020).

[13] A. Prasselsperger, M. Coughlan, N. Breslin, M. Yeung, C. Arthur, H. Donnelly, S. White, M. Afshari, M. Speicher, R. Yang *et al.*, Real-time electron solvation induced by bursts of laser-accelerated protons in liquid water, Phys. Rev. Lett. **127**, 186001 (2021).

[14] M.-C. Vozenin, J. Bourhis, and M. Durante, Towards clinical translation of flash radiotherapy, Nat. Rev. Clin. Oncol. **19**, 791 (2022).

[15] F. Kroll, F.-E. Brack, C. Bernert, S. Bock, E. Bodenstein, K. Brüchner, T. E. Cowan, L. Gaus, R. Gebhardt, U. Helbig *et al.*, Tumour irradiation in mice with a laser-accelerated proton beam, Nat. Phys. **18**, 316 (2022).

[16] J. Bin, L. Obst-Huebl, J.-H. Mao, K. Nakamura, L. D. Geulig, H. Chang, Q. Ji, L. He, J. De Chant, Z. Kober *et al.*, A new platform for ultra-high dose rate radiobiological research using the BELLA PW laser proton beamline, Sci. Rep. **12**, 1484 (2022).

[17] Y. Li, X. Shen, Y. Yao, S. Wu, A. Pukhov, and B. Qiao, Laser-driven time-limited light-sail acceleration of protons for tumor radiotherapy, Phys. Rev. Res. **5**, L012038 (2023).

[18] S. P. Hatchett, C. G. Brown, T. E. Cowan, E. A. Henry, J. S. Johnson, M. H. Key, J. A. Koch, A. B. Langdon, B. F. Lasinski, R. W. Lee *et al.*, Electron, photon, and ion beams from the relativistic interaction of petawatt laser pulses with solid targets, Phys. Plasmas **7**, 2076 (2000).

[19] E. L. Clark, K. Krushelnick, J. R. Davies, M. Zepf, M. Tatarakis, F. N. Beg, A. Machacek, P. A. Norreys, M. I. K. Santala, I. Watts *et al.*, Measurements of energetic proton transport through magnetized plasma from intense laser interactions with solids, Phys. Rev. Lett. **84**, 670 (2000).

[20] S. Wilks, A. Langdon, T. Cowan, M. Roth, M. Singh, S. Hatchett, M. Key, D. Pennington, A. MacKinnon, and R. Snavely, Energetic proton generation in ultra-intense laser-solid interactions, Phys. Plasmas **8**, 542 (2001).

[21] T. E. Cowan, J. Fuchs, H. Ruhl, A. Kemp, P. Audebert, M. Roth, R. Stephens, I. Barton, A. Blazevic, E. Brambrink *et al.*, Ultralow emittance, multi-MeV proton beams from a laser virtual-cathode plasma accelerator, Phys. Rev. Lett. **92**, 204801 (2004).

[22] J. Bin, W. Ma, K. Allinger, H. Wang, D. Kiefer, S. Reinhardt, P. Hilz, K. Khrennikov, S. Karsch, X. Q. Yan *et al.*, On the small divergence of laser-driven ion beams from nanometer thick foils, Phys. Plasmas **20**, 073113 (2013).

[23] H. Schwoerer, S. Pfotenhauer, O. Jäckel, K.-U. Amthor, B. Liesfeld, W. Ziegler, R. Sauerbrey, K. Ledingham, and T. Esirkepov, Laser-plasma acceleration of quasi-monoenergetic protons from microstructured targets, Nature (London) **439**, 445 (2006).

[24] T. Ziegler, I. Göthel, S. Assenbaum, C. Bernert, F.-E. Brack, T. E. Cowan, N. P. Dover, L. Gaus, T. Kluge, S. Kraft *et al.*, Laser-driven high-energy proton beams from cascaded acceleration regimes, Nat. Phys. **20**, 1211 (2024).

[25] C. N. Danson, C. Haefner, J. Bromage, T. Butcher, J.-C. F. Chanteloup, E. A. Chowdhury, A. Galvanauskas, L. A. Gizzi, J. Hein, D. I. Hillier *et al.*, Petawatt and exawatt class lasers worldwide, High Power Laser Sci. Eng. **7**, e54 (2019).

[26] K. Harres, M. Schollmeier, E. Brambrink, P. Audebert, A. Blažević, K. Flippo, D. Gautier, M. Geißel, B. Hegelich, F. Nürnberg *et al.*, Development and calibration of a Thomson parabola with microchannel plate for the detection of laser-accelerated MeV ions, Rev. Sci. Instrum. **79**, 093306 (2008).

[27] S. Reinhardt, W. Draxinger, J. Schreiber, and W. Assmann, A pixel detector system for laser-accelerated ion detection, J. Instrum. **8**, P03008 (2013).

[28] D. Haffa, R. Yang, J. Bin, S. Lehrack, F.-E. Brack, H. Ding, F. S. Englbrecht, Y. Gao, J. Gebhard, M. Gilljohann *et al.*, I-BEAT: Ultrasonic method for online measurement of the energy distribution of a single ion bunch, Sci. Rep. **9**, 6714 (2019).

[29] V. Scuderi, G. Milluzzo, D. Doria, A. Alejo, A. Amico, N. Booth, G. Cuttone, J. Green, S. Kar, G. Korn *et al.*, TOF diagnosis of laser accelerated, high-energy protons, Nucl. Instrum. Methods Phys. Res. A **978**, 164364 (2020).

[30] J. Metzkes, L. Karsch, S. Kraft, J. Pawelke, C. Richter, M. Schürer, M. Sobiella, N. Stiller, K. Zeil, and U. Schramm, A scintillator-based online detector for the angularly resolved measurement of laser-accelerated proton spectra, Rev. Sci. Instrum. **83**, 123301 (2012).

[31] M. Reimold, S. Assenbaum, C. Bernert, E. Beyreuther, F.-E. Brack, L. Karsch, S. D. Kraft, F. Kroll, M. Loeser, A. Nossula *et al.*, Time-of-flight spectroscopy for laser-driven proton beam monitoring, Sci. Rep. **12**, 21488 (2022).

[32] S. Gerlach, F. Balling, A. Schmidt, F. Brack, F. Kroll, J. Metzkes-Ng, M. Reimold, U. Schramm, M. Speicher, K. Zeil *et al.*, Three-dimensional acoustic monitoring of laser-accelerated protons in the focus of a pulsed-power solenoid lens, High Power Laser Sci. Eng. **11**, e38 (2023).

[33] P. Poole, C. Andereck, D. Schumacher, R. Daskalova, S. Feister, K. George, C. Willis, K. Akli, and E. Chowdhury, Liquid crystal films as on-demand, variable thickness (50–5000 nm) targets for intense lasers, Phys. Plasmas **21**, 063109 (2014).

[34] Y. Gao, J. Bin, D. Haffa, C. Kreuzer, J. Hartmann, M. Speicher, F. H. Lindner, T. M. Ostermayr, P. Hilz, T. F. Rösch *et al.*, An automated, 0.5 Hz nano-foil target positioning system for intense laser plasma experiments, High Power Laser Sci. Eng. **5**, e12 (2017).

[35] P. McKenna, K. Ledingham, I. Spencer, T. McCany, R. Singhal, C. Ziener, P. Foster, E. Divall, C. Hooker, D. Neely *et al.*, Char-

acterization of multiterawatt laser-solid interactions for proton acceleration, Rev. Sci. Instrum. **73**, 4176 (2002).

[36] N. Dover, M. Nishiuchi, H. Sakaki, K. Kondo, H. Lowe, M. Alkhimova, E. Ditter, O. Ettlinger, A. Y. Faenov, M. Hata *et al.*, Demonstration of repetitive energetic proton generation by ultra-intense laser interaction with a tape target, High Energy Density Phys. **37**, 100847 (2020).

[37] D. Levy, I. A. Andriyash, S. Haessler, J. Kaur, M. Ouillé, A. Flacco, E. Kroupp, V. Malka, and R. Lopez-Martens, Low divergence proton beams from a laser-plasma accelerator at kHz repetition rate, Phys. Rev. Accel. Beams **25**, 093402 (2022).

[38] L. Obst, S. Göde, M. Rehwald, F.-E. Brack, J. Branco, S. Bock, M. Bussmann, T. E. Cowan, C. B. Curry, F. Fiuza *et al.*, Efficient laser-driven proton acceleration from cylindrical and planar cryogenic hydrogen jets, Sci. Rep. **7**, 10248 (2017).

[39] M. Gauthier, C. Curry, S. Göde, F.-E. Brack, J. Kim, M. MacDonald, J. Metzkes, L. Obst, M. Rehwald, C. Rödel *et al.*, High repetition rate, multi-MeV proton source from cryogenic hydrogen jets, Appl. Phys. Lett. **111**, 114102 (2017).

[40] O. Seemann, Y. Wan, S. Tata, E. Kroupp, and V. Malka, Laser proton acceleration from a near-critical imploding gas target, Phys. Rev. Lett. **133**, 025001 (2024).

[41] A. Thoss, M. Richardson, G. Korn, M. Faubel, H. Stiel, U. Vogt, and T. Elsaesser, Kilohertz sources of hard x rays and fast ions with femtosecond laser plasmas, J. Opt. Soc. Am. B **20**, 224 (2003).

[42] M. Ekimova, W. Quevedo, M. Faubel, P. Wernet, and E. T. Nibbering, A liquid flatjet system for solution phase soft-x-ray spectroscopy, Struct. Dyn. **2**, 054301 (2015).

[43] J. T. Morrison, S. Feister, K. D. Frische, D. R. Austin, G. K. Ngirmang, N. R. Murphy, C. Orban, E. A. Chowdhury, and W. Roquemore, MeV proton acceleration at kHz repetition rate from ultra-intense laser liquid interaction, New J. Phys. **20**, 022001 (2018).

[44] P. Puyuelo-Valdes, D. de Luis, J. Hernandez, J. Apiñaniz, A. Curcio, J. Henares, M. Huault, J. Pérez-Hernández, L. Roso, G. Gatti *et al.*, Implementation of a thin, flat water target capable of high-repetition-rate MeV-range proton acceleration in a high-power laser at the CLPU, Plasma Phys. Control. Fusion **64**, 054003 (2022).

[45] F. Treffert, C. Curry, H.-G. Chou, C. Crissman, D. DePonte, F. Fiuza, G. Glenn, R. Hollinger, R. Nedbailo, J. Park *et al.*, High-repetition-rate, multi-MeV deuteron acceleration from converging heavy water microjets at laser intensities of 10^{21} W/cm^2, Appl. Phys. Lett. **121**, 074104 (2022).

[46] Y. H. Kim, H. Kim, S. C. Park, Y. Kwon, K. Yeom, W. Cho, T. Kwon, H. Yun, J. H. Sung, S. K. Lee *et al.*, High-harmonic generation from a flat liquid-sheet plasma mirror, Nat. Commun. **14**, 2328 (2023).

[47] Z. Cao, Z. Peng, Y. Shou, J. Zhao, S. Chen, Y. Gao, J. Liu, P. Wang, Z. Mei, Z. Pan *et al.*, Vibration and jitter of free-flowing thin liquid sheets as target for high-repetition-rate laser-ion acceleration, Front. Phys. **11**, 1172075 (2023).

[48] M. Füle, A. Kovács, T. Gilinger, M. Karnok, P. Gaál, S. Figul, G. Marowsky, and K. Osvay, Development of an ultrathin liquid sheet target for laser ion acceleration at high repetition rates in the kHz-range, High Power Laser Sci. Eng. **12**, e37 (2024).

[49] A. Watanabe, H. Saito, Y. Ishida, M. Nakamoto, and T. Yajima, A new nozzle producing ultrathin liquid sheets for femtosecond pulse dye lasers, Opt. Commun. **71**, 301 (1989).

[50] M. Kondoh and M. Tsubouchi, Liquid-sheet jets for terahertz spectroscopy, Opt. Express **22**, 14135 (2014).

[51] G. Taylor, Formation of thin flat sheets of water, Proc. R. Soc. Lond. A **259**, 1 (1961).

[52] M. Streeter, G. Glenn, S. DiIorio, F. Treffert, B. Loughran, H. Ahmed, S. Astbury, M. Borghesi, N. Bourgeois, C. Curry *et al.*, Stable laser-acceleration of high-flux proton beams with plasma collimation, Nat. Commun. **16**, 1004 (2025).

[53] J. Hartmann, D. Haffa, M. Speicher, J. Bin, P. Hilz, C. Kreuzer, T. Ostermayr, S. Lehrack, and J. Schreiber, The spatial contrast challenge for intense laser-plasma experiments, J. Phys.: Conf. Ser. **1079**, 012003 (2018).

[54] J. Hartmann, Quantitative Ion Spectrometry and first laser-ion acceleration results at the Centre for Advanced Laser Applications, Ph.D. thesis, Ludwig-Maximilians-Universität München, 2022.

[55] B. M. Hegelich, B. Albright, J. Cobble, K. Flippo, S. Letzring, M. Paffett, H. Ruhl, J. Schreiber, R. Schulze *et al.*, Laser acceleration of quasi-monoenergetic MeV ion beams, Nature (London) **439**, 441 (2006).

[56] P. Wang, Z. Gong, S. G. Lee, Y. Shou, Y. Geng, C. Jeon, I. J. Kim, H. W. Lee, J. W. Yoon, J. H. Sung *et al.*, Super-heavy ions acceleration driven by ultrashort laser pulses at ultrahigh intensity, Phys. Rev. X **11**, 021049 (2021).

[57] M. Zimmer, S. Scheuren, T. Ebert, G. Schaumann, B. Schmitz, J. Hornung, V. Bagnoud, C. Rödel, and M. Roth, Analysis of laser-proton acceleration experiments for development of empirical scaling laws, Phys. Rev. E **104**, 045210 (2021).

[58] J. Schreiber, F. Bell, and Z. Najmudin, Optimization of relativistic laser-ion acceleration, High Power Laser Sci. Eng. **2**, e41 (2014).

[59] F. Consoli, V. T. Tikhonchuk, M. Bardon, P. Bradford, D. C. Carroll, J. Cikhardt, M. Cipriani, R. J. Clarke, T. E. Cowan, C. N. Danson *et al.*, Laser produced electromagnetic pulses: generation, detection and mitigation, High Power Laser Sci. Eng. **8**, e22 (2020).

[60] D. J. Hoffman, T. B. Van Driel, T. Kroll, C. J. Crissman, E. S. Ryland, K. J. Nelson, A. A. Cordones, J. D. Koralek, and D. P. DePonte, Microfluidic liquid sheets as large-area targets for high repetition XFELS, Front. Mol. Biosci. **9**, 1048932 (2022).

[61] T. Esirkepov, M. Borghesi, S. V. Bulanov, G. Mourou, and T. Tajima, Highly efficient relativistic-ion generation in the laser-piston regime, Phys. Rev. Lett. **92**, 175003 (2004).

[62] A. Macchi, F. Cattani, T. V. Liseykina, and F. Cornolti, Laser acceleration of ion bunches at the front surface of overdense plasmas, Phys. Rev. Lett. **94**, 165003 (2005).

[63] A. Macchi, S. Veghini, and F. Pegoraro, "Light sail" acceleration reexamined, Phys. Rev. Lett. **103**, 085003 (2009).

[64] A. Döpp, C. Eberle, S. Howard, F. Irshad, J. Lin, and M. Streeter, Data-driven science and machine learning methods in laser-plasma physics, High Power Laser Sci. Eng. **11**, e55 (2023).

[65] R. Shalloo, S. Dann, J.-N. Gruse, C. Underwood, A. Antoine, C. Arran, M. Backhouse, C. Baird, M. Balcazar, N. Bourgeois *et al.*, Automation and control of laser wakefield accelerators using Bayesian optimization, Nat. Commun. **11**, 6355 (2020).